Catalysis
Science & Technology

RSCPublishing

PAPER

Cite this: *Catal. Sci. Technol.*, 2013, **3**, 1324

Catalytic conversion of syngas to mixed alcohols over CuFe-based catalysts derived from layered double hydroxides†

Wa Gao, Yufei Zhao, Junmin Liu, Qianwen Huang, Shan He, Changming Li, Jingwen Zhao and Min Wei*

Received 10th January 2013,
Accepted 5th February 2013

DOI: 10.1039/c3cy00025g

www.rsc.org/catalysis

A uniform and highly dispersed CuFe-based catalyst was obtained *via* a calcination–reduction process of a CuFeMg-layered double hydroxide (LDH) precursor, which exhibits good activity and selectivity towards catalytic conversion of syngas to mixed alcohols. X-ray diffraction (XRD) and scanning electron microscopy (SEM) reveal that the CuFeMg-LDH precursor possesses high crystallinity with a particle size of 40–60 nm. High resolution transmission electron microscopy (HRTEM) and scanning transmission electron microscopy (STEM) demonstrate a high dispersion of copper and iron species on the catalyst surface. The CuFe-based catalyst derived from CuFeMg-LDHs shows high CO conversion (56.89%) and the total alcohol yield (0.28 g $mL_{cat.}^{-1}$ h^{-1}), as a result of the high dispersion of active species as well as the synergistic effect between the copper and the iron species revealed by X-ray photoelectron spectra (XPS) and H_2 temperature-programmed reduction (H_2-TPR) techniques. Therefore, this work provides a facile and effective method for the preparation of CuFe-based catalysts with high catalytic activity, which can be potentially used in syngas conversion to mixed alcohols.

1. Introduction

Mixed alcohols from the catalytic conversion of syngas ($CO + H_2$) derived from coal, natural gas or renewable biomass have attracted considerable attention due to their potential applications as fuels, fuel additives, and intermediates for value-added chemicals including medicines, cosmetics and polyesters.[1–3] In the past decades, the alcohol synthesis catalysts have undergone a number of improvements related to better characterization for catalyst compositions and to enhancement of per-pass conversion, alcohol yield and product selectivity.[4] The noble metal-based catalysts, mainly Rh catalysts,[5–7] show good catalytic performance due to their unique CO adsorption behavior, but the very high cost restricts their large scale utilization. Therefore, non-noble metal-based catalysts, including modified methanol synthesis catalysts,[8–10] modified Fischer–Tropsch catalysts based on Co, Fe and Ni[11–16] as well as modified Mo-based catalysts,[17,18] have evoked increasing research interest.

Among these non-noble metal catalysts, modified Fischer–Tropsch synthesis catalysts (*e.g.*, CuFe[11,16] or CuCo[13,14] catalysts) are regarded as the promising candidates for mixed alcohol synthesis from syngas. However, CuCo-based catalysts generally suffer from poor stability in long-term run and the low total alcohol selectivity.[4] Although much effort has been devoted to the development of CuFe-based catalyst systems, several problems remain not well-resolved: catalyst deactivation, low alcohol productivity, insufficient selectivity, and a very complex mixture of reaction products.[2,4] For the di-metal or multi-metal catalysts, a homogeneous distribution of the active species and their distance play a key role in determining the catalyst activity and selectivity. One key obstacle of traditional multi-composition catalysts is that rapid deactivation will occur due to sintering/aggregation of active species. The agglomeration of one active species or separation of different active species would lead to a decrease in the synergistic effect and the resulting worse catalytic behavior.[4,19,20] Therefore, how to fabricate multi-composition catalysts with high efficiency, selectivity and stability towards alcohols is still a challenging goal.

Recently, considerable interest has been focused on layered double hydroxide (LDH) materials as heterogeneous catalysts or supports, as a result of their versatility in chemical composition and structural architecture.[21] LDHs are a large class of typical inorganic layered host materials which can be described by the

---

State Key Laboratory of Chemical Resource Engineering, Beijing University of Chemical Technology, Beijing 100029, P. R. China.
E-mail: weimin@mail.buct.edu.cn; Fax: +86-10-64425385; Tel: +86-10-64412131

† Electronic supplementary information (ESI) available. See DOI: 10.1039/c3cy00025g

general formula $[M^{2+}{}_{1-x}M^{3+}{}_{x}(OH)_2](A^{n-})_{x/n}\cdot mH_2O$ (M^{2+} and M^{3+} are divalent and trivalent metals, respectively; A^{n-} is the interlayer anion compensating for the positive charge of the brucite-like layers).[22] A unique structural characteristic of LDH materials is that the M^{2+} and M^{3+} cations are distributed in an ordered and uniform manner in the LDH layers, as verified by Grey *et al.* by means of multinuclear NMR spectroscopy.[23] Moreover, a topotactic transformation of LDH materials to metal oxides or metal–metal oxide composites occurs upon heating in air or under reducing conditions, respectively. This provides a facile method to obtain supported oxide or metal nanoparticles with multi-composition, high dispersion and specific morphology.

In this work, a CuFeMg-LDH precursor was synthesized by a simple and scale-up coprecipitation method developed by our group.[24] The advantage of this precursor material is that divalent copper and trivalent iron cations are uniformly distributed in slabs of edge-sharing MO_6 octahedra. After the calcination and reduction process, a homogeneous and highly-dispersed CuFe-based catalyst was obtained, which was revealed by XRD, HRTEM and STEM. H_2-TPR and XPS demonstrate a strong synergistic effect between copper and iron active species. The catalytic performances of the CuFe-based catalyst towards carbon monoxide hydrogenation were examined in a fixed bed microreactor; the maximal CO conversion reaches 56.89%, with a total alcohol yield of 0.28 g $mL_{cat.}{}^{-1}$ h^{-1}, superior to the CuFe-catalyst prepared by the conventional co-precipitation method. By virtue of the facile scale-up method and excellent catalytic activity, the CuFe-based catalysts derived from the CuFeMg-LDH precursor in this work can be prospectively applied as a promising candidate for carbon monoxide hydrogenation in C1 industry.

2. Experimental section

2.1 Materials

Analytical grade chemicals including $Cu(NO_3)_2\cdot 3H_2O$, $Fe(NO_3)_3\cdot 9H_2O$, $Mg(NO_3)_2\cdot 6H_2O$, NaOH and Na_2CO_3 were purchased from the Beijing Chemical Co. Limited and used without further purification. The deionized and decarbonated water was used in all the experimental processes.

2.2 Synthesis of CuFeMg-based catalysts

Three $Cu^{2+}Fe^{3+}Mg^{2+}$-LDH precursors with Cu : Fe : Mg molar ratios of 0.4 : 1.0 : 3.6, 1.6 : 1.0 : 3.7 and 2.5 : 1.0 : 3.7 (denoted as S_1-CuFeMg-LDH, S_2-CuFeMg-LDH and S_3-CuFeMg-LDH) were prepared by using a method that involves separate nucleation and aging steps (SNAS) developed in our laboratory.[24] This method consists of a very rapid mixing and nucleation process in a modified colloid mill, followed by a separate aging process. Solution A was a mixture of $Cu(NO_3)_2\cdot 3H_2O$, $Fe(NO_3)_3\cdot 9H_2O$ and $Mg(NO_3)_2\cdot 6H_2O$ with various Cu : Fe : Mg molar ratios dissolved in 100 mL of deionized water ($[Cu^{2+}] + [Mg^{2+}] + [Fe^{3+}] = 1.0$ M). Solution B was obtained by dissolving NaOH and Na_2CO_3 in the same volume of deionized water with [NaOH] = 1.6 M and $[CO_3{}^{2-}] = 2[Fe^{3+}]$. Solution A and B were simultaneously added to a colloid mill rotating at 3000 rpm and mixed for 2 min. The resulting slurry was removed from the colloid mill and aged at 393 K for 24 h. The final precipitate was filtered, washed thoroughly with deionized water and dried at 333 K for 24 h. The products were calcined in air at 873 K for 5 h with a heating rate of 2 K min^{-1} (denoted as S_1-CuFeMg-MMO, S_2-CuFeMg-MMO and S_3-CuFeMg-MMO). After hydrogen reduction at 623 K for 4 h with a heating rate of 5 K min^{-1}, these catalysts were labeled as S_1-CuFeMg-Cat, S_2-CuFeMg-Cat and S_3-CuFeMg-Cat.

The CuFeMg-LDHs were prepared by a conventional co-precipitation method and were used as reference samples (denoted as CP-CuFeMg-LDH). Typically, a mixture of copper, iron and magnesium nitrate was precipitated with an aqueous solution of $NH_3\cdot H_2O$ at 343 K and a constant pH of 7–8 in a well-stirred thermo-stated container. After aging for 2 h, the precipitate was washed thoroughly with distilled water, and was dried at 393 K for 12 h. The calcination and reduction process followed the same procedure described above (denoted as CP-CuFeMg-MMO and CP-CuFeMg-Cat).

2.3 Characterization of catalysts

X-ray diffraction (XRD) patterns of samples were obtained on a Shimadzu XRD-6000 diffractometer, using Cu Kα radiation (λ = 0.154 nm) at 40 kV, 30 mA, a scanning rate of 5° min^{-1}, a step size of 0.02° s^{-1}, and a 2θ angle ranging from 3 to 70°. The morphology of the CuFeMg-LDH was investigated using a scanning electron microscope (SEM; Zeiss Supra 55) with an accelerating voltage of 20 kV, combined with energy dispersive X-ray spectroscopy (EDX) for the determination of metal composition and elemental mapping. Transmission electron microscopy (TEM) was performed using a Hitachi H-800 transmission electron microscope operated at 100 kV. High resolution transmission electron microscopy (HRTEM) was carried out on a JEM-3010 at an accelerating voltage of 200 kV. The elemental analysis and high-resolution TEM investigation were carried out on a FEI Tecnai G2 F20 U-TWIN at an operating voltage of 200 keV. The specific surface area determination and pore volume analysis were performed by Brunauer–Emmett–Teller (BET) and Barret–Joyner–Halenda (BJH) methods using a Quantachrome Autosorb-1C-VP Analyzer. Prior to the measurements, the samples were degassed at 423 K for 10 h. X-ray photoelectron spectra (XPS) were recorded on a Thermo VG ESCALAB250 X-ray photoelectron spectrometer at a pressure of 2×10^{-9} Pa using Al Kα X-ray as the excitation source. H_2 temperature-programmed reduction (H_2-TPR) was carried out in a quartz reactor at atmospheric pressure. 0.1 g of sample was loaded in the middle of the reactor tube which was purged with N_2 at 473 K for 1 h. Then a reductive gas (5% H_2/Ar) was introduced at a flow rate of 40 mL min^{-1}. The temperature of the reactor was augmented linearly from 373 to 1173 K with a ramp of 10 K min^{-1} using a temperature-programmed controller. H_2 temperature-programmed desorption (H_2-TPD) was carried out on a Micromeritics TPD/TPR 2910 AutoChem instrument. The catalysts were pre-reduced in flowing 10 vol% H_2–He at 623 K for 4 h, cooled to ambient temperature, and flushed with He until the baseline was steady. Hydrogen was desorbed by heating the samples from 293 to 873 K at a rate of 5 K min^{-1} in flowing He.

2.4 Catalytic evaluation

Carbon monoxide hydrogenation reaction was carried out in a fixed bed stainless steel tubular microreactor (8 mm in diameter, 500 mm in length). The temperature of the reactor was controlled using a temperature controller. H_2, CO and N_2 were purged into the reactor at a desired rate using mass flow controllers. Nitrogen was used as an internal standard gas in the reactor feed. Prior to the reaction, the catalysts were reduced *in situ* in a flow of H_2 (40 mL min^{-1}) under atmospheric pressure at 623 K for 4 h. The catalytic evaluation was subsequently carried out in the tubular reactor by introducing the syngas (573 K, 4.0 MPa) after the pretreatment process. The reactor was cooled down to 573 K and synthesis gas with a flow rate of 40 mL min^{-1} (H_2: CO = 2.0, v/v) was introduced to increase the pressure to 4.0 MPa. During the process, the total pressure in the system was maintained at 4.0 MPa (H_2/CO = 2.0, v/v), and the space velocity was 2000 h^{-1}. The outlet gas components (CO, H_2, CH_4, CO_2 and N_2) and C_1–C_5 hydrocarbons were determined using an online GC-2014C Shimadzu gas chromatograph with a TCD detector (TDX-1 column) and an FID detector (Porapak Q column), respectively. The liquid hydrocarbons and alcohol products were captured using an ice-water bath and analyzed off-line using the same chromatograph (a PEG-20 M capillary column and a FID detector).

3. Results and discussion

3.1 Structural and morphological study of the catalysts

The XRD patterns of CuFeMg-LDH precursors with various Cu : Fe : Mg molar ratios are shown in Fig. 1A. In each case, the XRD pattern exhibits the characteristic reflections of LDH materials with a series of (00*l*) peaks appearing as narrow symmetric lines at low angle, corresponding to the basal spacing and higher order reflections.[25] After calcination in air at 873 K, the LDHs transform to a mixture of oxide and spinel phase (Fig. 1B: S_n-CuFeMg-MMO). The diffraction reflections at 2θ of 35.5° and 38.7° indicate the formation of CuO phase (JCPDS card no. 48-1548). The reflections at 2θ of 34.7°, 35.9°, and 62.2° correspond to a $CuFe_2O_4$ spinel phase (JCPDS card no. 34-0425). Meanwhile, MgO phase (JCPDS card no. 04-0829) and a trace amount of Fe_2O_3 (JCPDS card no. 33-0664) were identified in the XRD pattern. For the S_1-CuMgFe-MMO sample, no CuO phase was observed, possibly owing to a low Cu content in the precursor. The CuO phase appears in the S_2-CuFeMg-MMO sample and the reflection intensity increases significantly in the S_3-CuFeMg-MMO sample, as a result of the gradual increase in Cu content. The final S_n-CuFeMg-Cat samples obtained *via* a reduction process of CuFeMg-MMO are displayed in Fig. 1C. The strong peaks at 2θ of 43.3°, 50.4° and 74.1° were observed for S_2-CuFeMg-Cat and S_3-CuFeMg-Cat, corresponding to the (111), (200) and (220) reflections of Cu^0 crystalline phase (JCPDS card no. 4-0836). For the S_1-CuFeMg-Cat, however, no Cu^0 phase was detected, indicating that copper species present in this sample exists as an amorphous state or below the detection limit of XRD. Moreover, both the MgO phase and $CuFe_2O_4$ phase were still identified for the three catalysts. In addition, a diffraction peak at 44.7° for metallic Fe (JCPDS card no. 06-0696) was observed for all the three catalysts, whose intensity decreases from S_1-CuFeMg-Cat to S_3-CuFeMg-Cat. This is in accordance with the sequence of Fe content for the three samples. Based on the XRD results, it is concluded that the

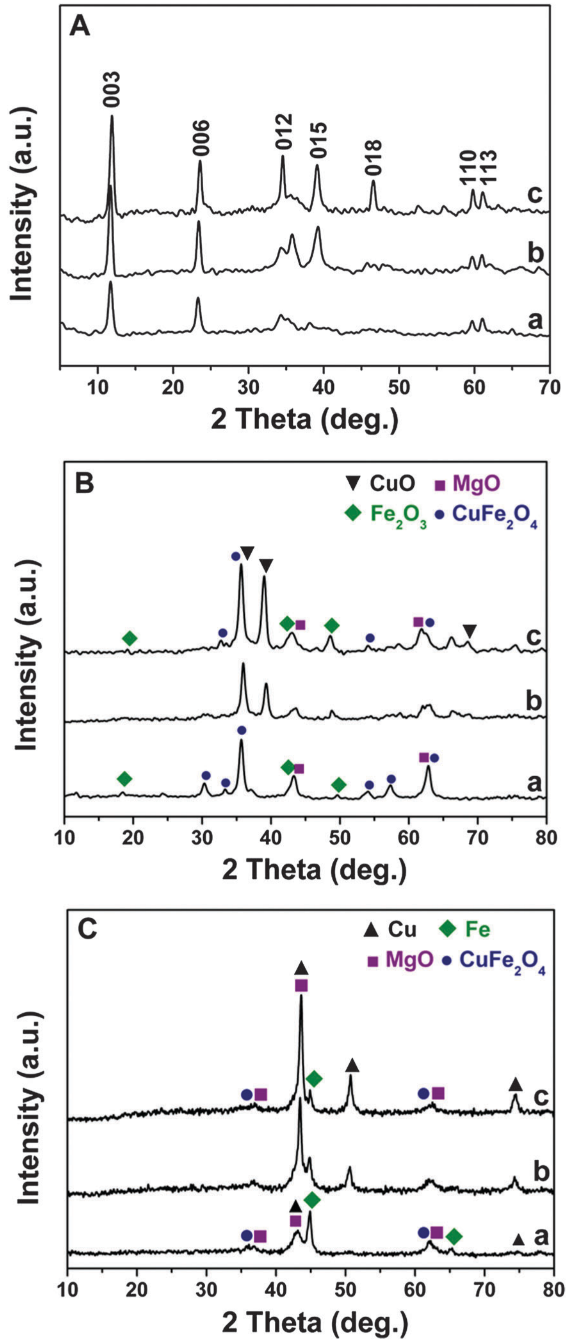

Fig. 1 (A) XRD patterns of CuFeMg-LDH precursors: (a) S_1-CuFeMg-LDH, (b) S_2-CuFeMg-LDH, and (c) S_3-CuFeMg-LDH; (B) XRD patterns of (a) S_1-CuFeMg-MMO, (b) S_2-CuFeMg-MMO, and (c) S_3-CuFeMg-MMO; (C) XRD patterns of (a) S_1-CuFeMg-Cat, (b) S_2-CuFeMg-Cat, and (c) S_3-CuFeMg-Cat.

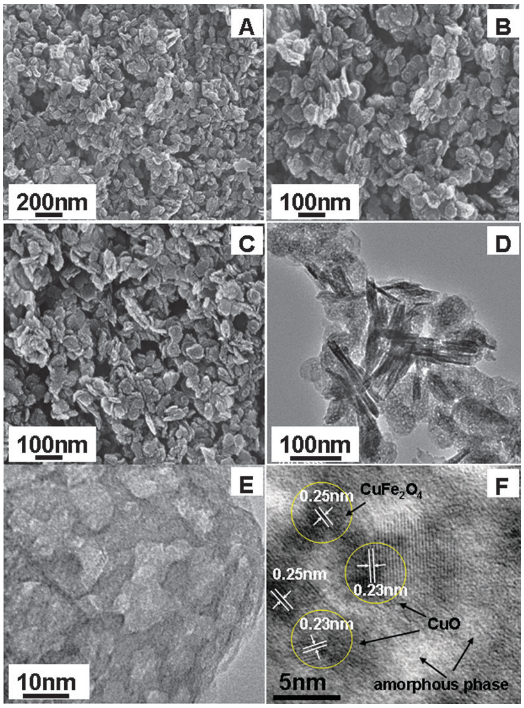

Fig. 2 SEM images of (A) S_2-CuFeMg-LDH, (B) S_2-CuFeMg-MMO, and (C) S_2-CuFeMg-Cat. (D), (E), and (F) HRTEM images of S_2-CuFeMg-MMO with different magnifications.

CuFeMg-LDH precursor transforms to a composite material consisting of CuO, Fe_2O_3, $CuFe_2O_4$, and MgO phase after a calcination process, and a subsequent phase transformation to Cu, Fe, MgO and $CuFe_2O_4$ phase after the following reduction procedure.

The morphology of S_2-CuFeMg-LDH, S_2-CuFeMg-MMO and S_2-CuFeMg-Cat samples revealed by SEM and HRTEM is shown in Fig. 2. SEM images of the CP-CuFeMg-LDH material (Fig. S1, ESI†) show a broad particle size ranging 50 nm–3 μm. In contrast, numerous well-defined LDH nanoplatelets with a narrow particle size of 40–60 nm are apparently observed by the separate nucleation and aging steps (SNAS) approach (Fig. 2A), which is a key feature in controlling the crystalline size distribution of this method. Fig. 2B and C show the SEM images of the resulting calcination and reduction product, which maintain the plate-like morphology of the original precursor. HRTEM was employed to reveal the structure of the S_2-CuFeMg-MMO sample. Some nanoparticles uniformly embedded in the platelet matrix are clearly observed (Fig. 2E). A typical HRTEM image of the nanoparticles shows two identified reflection patterns with interplanar distances of 0.23 and 0.25 nm (Fig. 2E), corresponding to the (111) plane of CuO phase and (211) plane of $CuFe_2O_4$ phase,[26] respectively. This observation is in agreement with the XRD results.

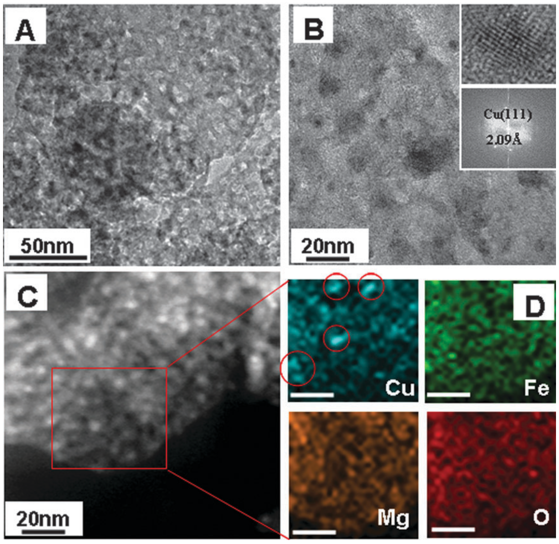

Fig. 3 (A) TEM, (B) HRTEM (inset: a single-crystalline Cu nanoparticle and corresponding Fourier transform image), and (C) HADDF-STEM image of the S_2-CuFeMg-Cat sample; (D) elemental mapping images of Cu, Fe, Mg and O for the S_2-CuFeMg-Cat sample; the scale bar is 20 nm.

The morphological features of the resulting reduction product, S_2-CuFeMg-Cat, are shown in Fig. 3. Abundant nanoparticles are observed on the surface of the nanoflake substrate, with a particle size of ∼5 nm (Fig. 3A and B); Fourier transform images (Fig. 3B, inset) reveal the presence of lattice fringes of 2.09 Å, corresponding to the (111) plane of the metallic copper.[27] In order to confirm the compositional distribution of the S_2-CuFeMg-Cat sample, elemental mapping analysis was performed by high-angle annular dark-field scanning TEM-energy-dispersive X-ray spectroscopy (HAADF-STEM-EDS). Fig. 3C and D display the elemental maps of Cu, Fe, Mg and O, respectively, from which a uniform and homogeneous distribution of these species is observed.

Fig. 4 displays the N_2 adsorption–desorption isotherm and the corresponding pore size distribution curve for the S_n-CuFeMg-Cat samples. All the three samples exhibit a typical IV isotherm with an H_3-type hysteresis loop ($P/P_0 > 0.4$), indicating the presence of mesopores. Furthermore, no any limiting adsorption at higher P/P_0 was observed, indicative of the existence of macropores.[28]

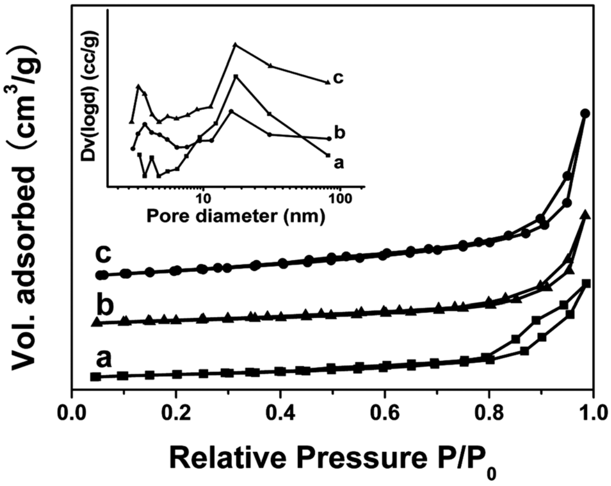

Fig. 4 N_2 adsorption–desorption curves and pore size distributions (inset) of (a) S_1-CuFeMg-Cat, (b) S_2-CuFeMg-Cat and (c) S_3-CuFeMg-Cat.

Table 1 Characterization of the CP-CuFeMg-Cat and S_n-CuFeMg-Cat samples

Samples	BET surface area (m^2 g^{-1})	BJH pore volume (cm^3 g^{-1})	Pore diameter (nm)
S_1-CuFeMg-Cat	50.32	1.23	3.4
S_2-CuFeMg-Cat	83.22	0.89	3.7
S_3-CuFeMg-Cat	53.99	0.79	3.3
CP-CuFeMg-Cat	11.55	0.04	3.8

This result is further confirmed by the corresponding wide distribution of pore size (Fig. 4, inset), resulting from stacking of LDH nanoflakes. In comparison with the CP-CuFeMg-Cat prepared by the conventional co-precipitation method, the S_n-CuFeMg-Cat samples show a much larger specific surface area (50.32–83.22 m^2 g^{-1}) and pore volume (0.79–1.23 cm^3 g^{-1}). The increased surface area and pore volume can be attributed to the uniform and narrow distribution of nanoplatelets, which would be beneficial for the improvement of catalytic activity (Table 1).

3.2 Evaluation of the catalytic behavior

The catalytic performance of the S_n-CuFeMg-Cat samples towards CO hydrogenation was examined under the following reaction conditions: 4.0 MPa, 573 K, GHSV of 2000 h^{-1}, $n(H_2)/n(CO) = 2.0$, in comparison with the CP-CuFeMg-Cat sample. The CO conversion, selectivity towards total alcohols, hydrocarbon and CO_2 are presented in Table 2. It can be seen that the CP-CuFeMg-Cat sample exhibits a low activity (CO conversion: 51.46%) and total alcohol selectivity (29.16%). In contrast, the S_n-CuFeMg-Cat samples exhibit largely enhanced catalytic behavior: the total alcohol selectivity increases gradually from 29.16% (CP-CuFeMg-Cat) to 49.07% (S_2-CuFeMg-Cat). The catalytic performance of the S_n-CuFeMg-Cat samples with varying molar ratios of Cu/Fe is also depicted in Table 2. The space-time yield (STY) of the alcohol products increases with the enhancement of the Cu/Fe ratio up to 1.6, and then decreases with a further increase in Cu content. The S_2-CuFeMg-Cat sample (Cu/Fe = 1.6) displays the largest STY among all the catalysts (0.28 g $mL_{cat.}^{-1}$ h^{-1}) as well as a high CO conversion (56.89%), which is superior to other Cu–Fe catalysts reported previously.[11,16] The product distributions are listed in Table 3. The alcohol products comprise C_1–C_6 linear mixed alcohols as expected; the main hydrocarbon products are olefin and paraffin. The alcohols as well as hydrocarbon products obtained over the S_n-CuFeMg catalysts obey Anderson–Schulz–Flory (ASF) carbon number distributions. An example of such distributions is displayed in Fig. 5 for the S_2-CuFeMg-Cat sample. The chain growth probability (α) is larger than zero but less than one because a part of intermediates desorb from the catalyst surface in each step of the carbon chain growth. Therefore, the yield of each alcohol in the products decreases with the increase of carbon chain according to the ASF distribution.[29,30] The carbon number distributions of linear alcohols and C_{4+} hydrocarbons are in good agreement with the ASF rule (Fig. 5), although C_2 and C_3 hydrocarbons deviate from the ASF distribution. It was found that the hydrocarbons and alcohols have rather close α values over the S_2-CuFeMg-Cat catalyst, indicating that they originate from the same intermediate.[31]

Table 2 Catalytic performance of CuFeMg catalysts

Catalysts	CO conversion (%)	STY (g $mL_{cat.}^{-1}$ h^{-1}) ROH[a]	HC[a]	Selectivity[b] (%) ROH	HC	CO_2
S_1-CuFeMg-Cat	63.22	0.21	0.35	32.77	54.34	12.89
S_2-CuFeMg-Cat	56.89	0.28	0.22	49.07	38.52	12.41
S_3-CuFeMg-Cat	50.32	0.24	0.19	45.75	39.57	14.68
CP-CuFeMg-Cat	51.46	0.16	0.30	29.16	58.91	11.93

Reaction conditions: $P = 4.0$ MPa, $T = 573$ K, GHSV = 2000 h^{-1}, $n(H_2)/n(CO) = 2.0$.[a] ROH for total alcohols and HC for hydrocarbon. [b] Selectivity based on the number of atoms per gram carbon = [number of CO converted to given product/total number of CO converted] × 100%.

Table 3 Product distributions of CuFeMg catalysts

Catalysts	ROH[a] (wt%) MeOH	EtOH	C_3OH	C_4OH	$C_{5+}OH$	HC[a] (wt%) CH_4	$C_{2-4}H$	$C_{5+}H$
S_1-CuFeMg-Cat	27.32	24.67	16.91	12.15	18.95	40.26	28.39	31.35
S_2-CuFeMg-Cat	33.04	28.96	14.68	12.07	11.25	37.91	32.61	29.48
S_3-CuFeMg-Cat	45.44	23.63	15.20	8.19	7.54	32.30	37.86	29.84
CP-CuFeMg-Cat	40.61	28.54	12.38	11.52	6.95	34.12	29.35	36.53

Reaction conditions: $P = 4.0$ MPa, $T = 573$ K, GHSV = 2000 h^{-1}, $n(H_2)/n(CO) = 2.0$. [a] ROH for total alcohols and HC for hydrocarbon.

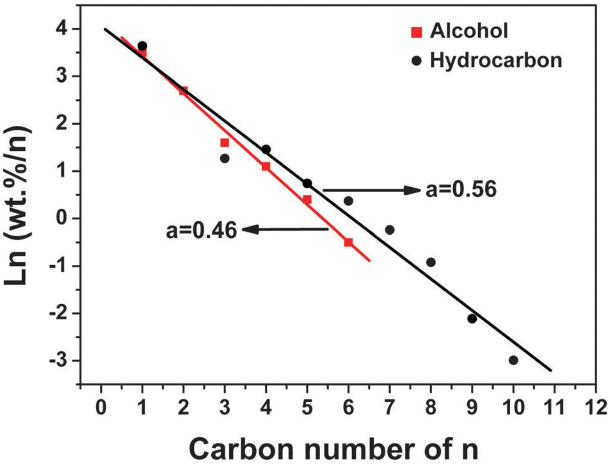

Fig. 5 ASF plots for the distributions of alcohols and hydrocarbons over the S_2-CuFeMg-Cat.

In the process of mixed alcohol synthesis from syngas over CuFe-based catalysts, the major reaction is the alcohol formation, while hydrocarbon formation and water-gas-shift reaction are the side reactions. On the basis of results reported previously,[2,3,32,33] mixed alcohols and hydrocarbons can be produced by the CO insertion mechanism over CuFe-based catalysts. Hydrogenation of the adsorbed formyl species would produce adsorbed alkyl species (CH_x). The carbon-chain growth of the alkyl group (C_nH_z) is propagated *via* CH_x addition; C_nH_z hydrogenation reaction will lead to the formation of hydrocarbon products. CO insertion into the metal–alkyl bond can form an acyl intermediate (CH_xCO) which undergoes a further hydrogenation to higher alcohol products. The production of mixed alcohols requires the synergetic effect of homogeneously dispersed iron and copper species, since Cu facilitates the dissociative chemisorption of H_2 and the associative adsorption of CO, while Fe induces the dissociative adsorption of CO and hydrogenation.[4,11,16,34] The synergistic effect of Cu and Fe plays a key role in determining the catalytic performance, which will be discussed in the next section.

The stability of the S_2-CuFeMg-Cat catalyst was also studied. Its XRD pattern after catalytic reaction (573 K, 48 h) is shown in Fig. S2 (ESI†), in which metallic Cu, metallic Fe, $CuFe_2O_4$ and MgO are identified. Compared with the fresh S_2-CuFeMg-Cat sample (Fig. 1C, curve b), the used catalyst shows significantly enhanced intensity of the $CuFe_2O_4$ reflections, implying the occurrence of a synergistic effect between copper and iron during the reaction. The EDX elemental mapping (Fig. S3, ESI†) of the used S_2-CuFeMg-Cat sample displays that Cu, Fe and Mg are homogeneously distributed in the catalyst, similar to the fresh one (Fig. 3). The HRTEM image (Fig. S4, ESI†) reveals that the Cu nanoparticles remain spherical in shape without an obvious change in size. The results indicate that the S_2-CuFeMg-Cat sample possesses a high stability upon reaction.

3.3 Cu–Fe synergistic effect and its correlation with activity

The Cu–Fe synergistic effect plays an important role in the high activity of mixed alcohol synthesis as reported previously.[2,4,12,16] To provide further insight into the synergistic effect of iron and copper, H_2-TPR measurement was performed. Fig. 6 shows the TPR profiles of the three S_n-CuFeMg-MMO samples, with pristine CuO and $CuFe_2O_4$ as reference samples. Pristine CuO gives rise to one broad peak in the temperature range 420–600 K, which is assigned to the reduction of CuO to Cu.[35,36] For the $CuFe_2O_4$ sample, the peaks in the temperature range 490–710 K in Fig. 6 (curve b) are ascribed to the reduction of $CuFe_2O_4$ to metallic Cu and Fe_2O_3, followed by the subsequent reduction of Fe_2O_3 to Fe_3O_4. It is hard to define a clear boundary between each of the reduction steps.[36,37] In the case of the three S_n-CuFeMg-MMO samples, two reduction processes were observed at low and high temperature range. For the S_1-CuFeMg-MMO sample, the strong reduction peak at 447 K in the low temperature range is ascribed to the reduction of $CuFe_2O_4$ to metallic Cu and Fe_3O_4. For the S_2-CuFeMg-MMO and S_3-CuFeMg-MMO sample, the first shoulder peak (at 476 K, 441 K) is due to the reduction of CuO to metallic Cu, while the subsequent strong peak (at 499 K, 473 K) is attributed to the reduction of $CuFe_2O_4$ to metallic Cu and Fe_3O_4. The peak appearing in the high temperature range 600–1200 K for all the S_n-CuFeMg-MMO samples could be assigned to the continuous reduction of iron oxides to metallic Fe *via* FeO.[38] Obviously, compared with the pristine CuO sample, the reduction peak of CuO in the S_n-CuFeMg-MMO samples shifts to a lower temperature, implying that the presence of Fe improves the reducibility of CuO. Moreover, the reduction temperature of $CuFe_2O_4$ in the S_n-CuFeMg-MMO samples decreases significantly in comparison with that of the pristine $CuFe_2O_4$ sample. The results suggest that a strong synergistic effect between copper and iron occurs in the CuFeMg-MMO samples,[39] which impose a beneficial influence on their hydrogenation performance.

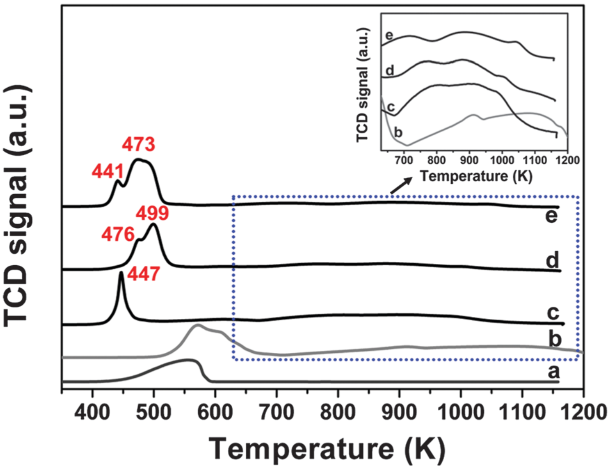

Fig. 6 Temperature-programmed reduction profiles of (a) CuO, (b) $CuFe_2O_4$, (c) S_1-CuFeMg-MMO, (d) S_2-CuFeMg-MMO, and (e) S_3-CuFeMg-MMO.

To further clarify the synergistic effect between copper and iron, XPS studies of Cu 2p and Fe 2p for the S_2-CuFeMg-LDH precursor, S_2-CuFeMg-MMO and S_2-CuFeMg-Cat were carried out (Fig. 7). For the S_2-CuFeMg-LDH precursor, binding energies of Cu $2p_{3/2}$ and Cu $2p_{1/2}$ are observed at ~935.4 and ~955.3 eV, respectively, indicative of $Cu(OH)_2$ species.[40] For the calcined sample, two peaks at ~931.9 and ~951.7 eV are attributed to the Cu $2p_{3/2}$ and Cu $2p_{1/2}$, respectively, with satellite peaks observed at ~941.5 and ~961.7 eV, corresponding to a Cu^{2+} state with a d^9 electron configuration. As shown in Fig. 7A (inset), the asymmetric Cu $2p_{3/2}$ peak can be deconvoluted into two contributions centered at ~931.9 and ~933.4 eV, which are due to the CuO and $CuFe_2O_4$, respectively.[41,42] In the case of the S_2-CuFeMg-Cat sample, the binding energies of Cu $2p_{3/2}$ and Cu $2p_{1/2}$ are located at 931.6 and 951.5 eV, respectively, in accordance with those of metallic copper.[43] The disappearance of the satellite peaks verifies the absence of Cu^{2+} species after the reduction process.

Fig. 7B displays the XPS spectra of Fe $2p_{3/2}$ for the three samples. The Fe $2p_{3/2}$ core level at 714.4 eV in the LDH precursor unambiguously confirms the presence of an Fe^{3+} state.[44] After calcination, the obtained S_2-CuFeMg-MMO sample shows two distinguishable main peaks at ~711.2 (Fe $2p_{3/2}$) and ~724.3 eV (Fe $2p_{1/2}$), indicating the presence of the Fe^{3+} cation.[45] After reduction, the Fe $2p_{3/2}$ peak shifts towards lower binding energy, coupled with the appearance of a peak at 710.6 eV, which can be identified as Fe_3O_4.[43] An inconspicuous peak observed at 706.94 eV implies the presence of Fe^0 on the surface.[46] It should be noted that the Cu $2p_{3/2}$ binding energy of the CuFeMg-MMO catalyst shifts toward a low energy of 1.4 eV in comparison with that of pristine CuO (933.3 eV), which also indicates the synergistic effect between iron and copper, in accordance with the results of TPR (Fig. 6). Based on the results of XRD, TEM and XPS, it is concluded that for the S_2-CuFeMg-Cat sample, copper species exists as a metallic state and iron species exists in a mixture of 0, +2 and +3 states.

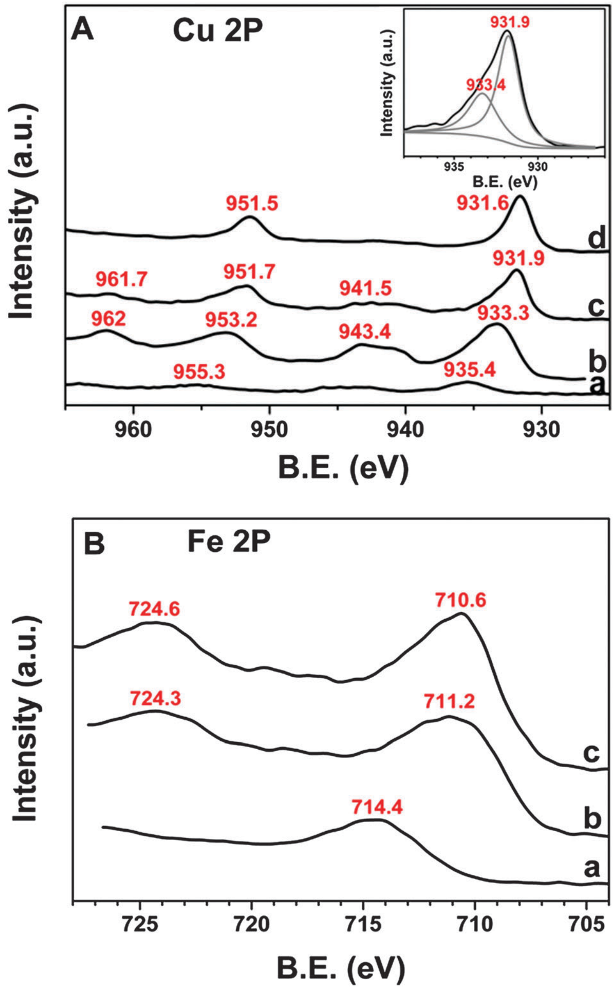

Fig. 7 (A) Cu 2p XPS spectra of (a) S_2-CuFeMg-LDH precursor, (b) CuO, (c) S_2-CuFeMg-MMO, and (d) S_2-CuFeMg-Cat; (B) Fe 2p XPS spectra of (a) S_2-CuFeMg-LDH precursor, (b) S_2-CuFeMg-MMO, and (c) S_2-CuFeMg-Cat.

Fig. 8 displays H_2-TPD profiles of the three S_n-CuFeMg-Cat catalysts and the comparison sample CP-CuFeMg-Cat. In the temperature range 350–800 K, the desorption of H_2 can be assigned to two different adsorbed H species: the desorption peak at low temperature (350–500 K, H_α) is attributed to hydrogen desorption from Cu sites;[44] the peak at high temperature (600–800 K, H_β) corresponds to the hydrogen desorption from Fe sites.[47,48] Obviously, both the hydrogen desorption peaks for the S_n-CuFeMg-Cat catalysts move to higher temperature compared with those for the CP-CuFeMg-Cat sample, indicating that a higher activation of H_2 occurs on the surface of S_n-CuFeMg-Cat and a stronger metal–hydrogen bonding is formed. This is due to the high dispersion of Fe and Cu species in the S_n-CuFeMg-Cat samples, which affords more unsaturated coordination centers for the hydrogen adsorption. It has been reported that the activation of H_2 plays an essential role in promoting the catalytic activity.[4,47,48] In addition, the S_2-CuFeMg-Cat sample exhibits the highest H_α and H_β desorption temperature, indicating the strongest metal–hydrogen interaction, which agrees well with its highest catalytic activity.

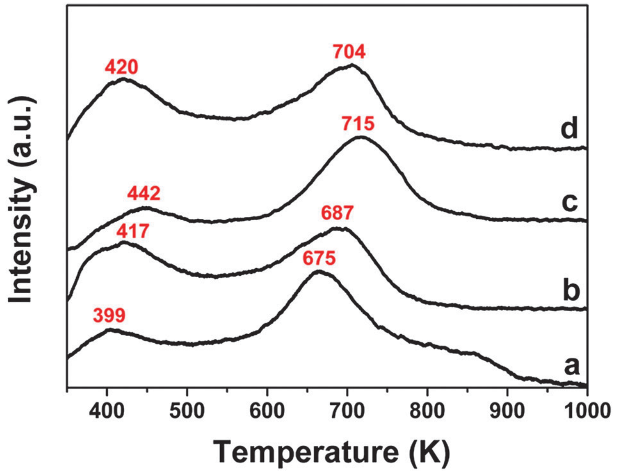

Fig. 8 H_2-TPD curves of (a) CP-CuFeMg-Cat, (b) S_1-CuFeMg-Cat, (c) S_2-CuFeMg-Cat, and (d) S_3-CuFeMg-Cat.

4. Conclusions

In summary, a series of CuFe-based catalysts were synthesized by a scale-up method (SNAS) following a calcination–reduction process, which display high catalytic activity for the synthesis of mixed alcohols from syngas. The S_2-CuFeMg-Cat sample exhibits rather high CO conversion (56.89%), high selectivity towards higher alcohols (49.07%) as well as the total alcohol yield (0.28 g $mL_{cat.}{}^{-1}$ h^{-1}), superior to the CuFe-catalyst prepared by the conventional co-precipitation method. The desirable carbon monoxide hydrogenation activity of the S_2-CuMgFe-Cat catalyst is attributed to: (1) a homogeneous and high distribution of copper and iron active sites which provides more unsaturated coordination centers for the hydrogen and CO adsorption; (2) a strong synergistic effect between iron and copper species, which contributes to the enhancement of selectivity towards alcohols. This work provides a facile method for the preparation of highly-dispersed CuFe-based catalysts *via* the approach of the LDH precursor, which serve as a good candidate in CO hydrogenation. It is expected that this strategy can be extended to the fabrication of other highly-dispersed multi-metal catalysts with significantly enhanced catalytic behavior.

Acknowledgements

This work was supported by the 973 Program (Grant No. 2011CBA00504), the National Natural Science Foundation of China (NSFC) and the Collaboration Project from the Beijing Education Committee. M. Wei particularly appreciates the financial aid from the China National Funds for Distinguished Young Scientists of the NSFC.

Notes and references

1 R. G. Herman, *Catal. Today*, 2000, **55**, 233–245.
2 V. Subramani and S. K. Gangwal, *Energy Fuels*, 2008, **22**, 814–839.

3 J. J. Spivey and A. Egbebi, *Chem. Soc. Rev.*, 2007, **36**, 1514–1528.

4 K. G. Fang, D. B. Li, M. G. Lin, M. L. Xiang, W. Wei and Y. H. Sun, *Catal. Today*, 2009, **147**, 133–138.

5 Z. L. Fan, W. Chen, X. L. Pan and X. H. Bao, *Catal. Today*, 2009, **147**, 86–93.

6 D. H. Mei, R. Rousseau, S. M. Kathmann, V. A. Glezakou, M. H. Engelhard, W. L. Jiang, C. M. Wang, M. A. Gerber, J. F. White and D. J. Stevens, *J. Catal.*, 2010, **271**, 325–342.

7 G. Prieto, P. Concepcion, A. Martinez and E. Mendoza, *J. Catal.*, 2011, **280**, 274–288.

8 W. S. Epling, G. B. Hoflund and D. M. Minahan, *J. Catal.*, 1998, **175**, 175–184.

9 A. Beretta, Q. Sun, R. G. Herman and K. Klier, *Ind. Eng. Chem. Res.*, 1996, **35**, 1534–1542.

10 M. T. Xu, M. J. L. Gines, A. M. Hilmen, B. L. Stephens and E. Iglesia, *J. Catal.*, 1997, **171**, 130–147.

11 M. G. Lin, K. G. Fang, D. D. Li and Y. H. Sun, *Catal. Commun.*, 2008, **9**, 1869–1873.

12 R. Xu, W. Wei, W. H. Li, T. D. Hu and Y. H. Sun, *J. Mol. Catal. A: Chem.*, 2005, **234**, 75–83.

13 X. Dong, X. L. Liang, H. Y. Li, G. D. Lin, P. Zhang and H. B. Zhang, *Catal. Today*, 2009, **147**, 158–165.

14 N. T. Thao, M. H. Z. Niaki, H. Alamdari and S. Kaliaguine, *J. Catal.*, 2007, **245**, 348–357.

15 N. D. Subramanian, G. Balaji, C. S. S. R. Kumar and J. J. Spivey, *Catal. Today*, 2009, **147**, 100–106.

16 Y. W. Lu, F. Yu, J. Hu and J. Liu, *Appl. Catal., A*, 2012, **429**, 48–58.

17 M. Xiang, D. Li, W. Li, B. Zhong and Y. Sun, *Catal. Commun.*, 2007, **8**, 503–507.

18 H. Shou, D. Ferrari, D. G. Barton, C. W. Jones and R. J. Davis, *ACS Catal.*, 2012, **2**, 1408–1416.

19 X. M. Yang, Y. Wei, L. P. Zhou and Y. L. Su, *Fuel Process. Technol.*, 2010, **91**, 1168–1173.

20 (*a*) A. Ota, E. L. Kunkes, I. Kasatkin, E. Groppo, D. Ferri, B. Poceiro, R. M. N. Yerga and M. Behrens, *J. Catal.*, 2012, **293**, 27–38; (*b*) S. C. Yang, W. N. Su, S. D. Lin, J. Ricka and B. J. Hwang, *Catal. Sci. Technol.*, 2012, **2**, 807–812; (*c*) S. Esposito, M. Turco, G. Bagnasco, C. Cammarano, P. Pernice and A. Aronne, *Appl. Catal., A*, 2010, **372**, 48–57; (*d*) Y. N. Wang, X. P. Duan, J. W. Zheng, H. Q. Lin, Y. Z. Yuan, H. Ariga, S. Takakusagi and K. Asakura, *Catal. Sci. Technol.*, 2012, **2**, 1637–1639.

21 (*a*) M. Q. Zhao, Q. Zhang, W. Zhang, J. Q. Huang, Y. Zhang, D. S. Su and F. Wei, *J. Am. Chem. Soc.*, 2010, **132**, 14739–14741; (*b*) J. A. Gursky, S. D. Blough, C. Luna, C. Gomez, A. N. Luevano and E. A. Gardner, *J. Am. Chem. Soc.*, 2006, **128**, 8376–8377; (*c*) Y. Tang, Y. Liu, P. Zhu, Q. S. Xue, L. Chen and Y. Lu, *AIChE J.*, 2009, **55**, 1217–1228; (*d*) B. T. Mesheshaa, N. Barrabésb, K. Föttingerb, R. J. Chimentãoa, J. Llorcac, F. Medinaa, G. Rupprechterb and J. E. Sueirasa, *Appl. Catal., B*, 2012, **117–118**, 236–245; (*e*) Y. Zhao, P. Chen, B. Zhang, D. S. Su, S. Zhang, L. Tian, J. Lu, Z. Li, X. Cao, B. Wang, M. Wei, D. G. Evans and X. Duan, *Chem.–Eur. J.*, 2012, **18**, 11949–11958; (*f*) P. Gao, F. Li, F. K. Xiao, N. Zhao, N. N. Sun, W. Wei, L. S. Zhong and Y. H. Sun, *Catal. Sci. Technol.*, 2012, **2**, 1447–1454.

22 (*a*) J. A. Gursky, S. D. Blough, C. Luna, C. Gomez, A. N. Luevano and E. A. Gardner, *J. Am. Chem. Soc.*, 2006, **128**, 8376–8377; (*b*) G. R. Williams and D. O'Hare, *J. Mater. Chem.*, 2006, **16**, 3065–3074; (*c*) A. M. Fogg, A. L. Rohl, G. M. Parkinson and D. O'Hare, *Chem. Mater.*, 1999, **11**, 1194–1200; (*d*) L. Li, Y. Feng, Y. Li, W. Zhao and J. Shi, *Angew. Chem., Int. Ed.*, 2009, **48**, 5888.

23 P. J. Sideris, U. G. Nielsen, Z. H. Gan and C. P. Grey, *Science*, 2008, **321**, 113–117.

24 (*a*) Y. Zhao, F. Li, R. Zhang, D. G. Evans and X. Duan, *Chem. Mater.*, 2002, **14**, 4286–4291; (*b*) Y. Zhao, S. Zhang, B. Li, H. Yan, L. Tian, W. Shi, M. Wei, D. G. Evans and X. Duan, *Chem.–Eur. J.*, 2011, **17**, 13175–13181.

25 (*a*) Y. Kobayashi, X. L. Ke, H. Hata, P. Schiffer and T. E. Mallouk, *Chem. Mater.*, 2008, **20**, 2374–2381; (*b*) J. Pisson, C. Taviot-Gueho, Y. Israeli, F. Leroux, P. Munsch, J. P. Itie, V. Briois, N. Morel-Desrosiers and J. P. Besse, *J. Phys. Chem. B*, 2003, **107**, 9243–9248.

26 K. H. Lee, B. Lee, K. R. Lee, M. H. Yi and N. H. Hur, *Chem. Commun.*, 2012, **48**, 4414–4416.

27 N. Barrabes, D. Cornado, K. Foettinger, A. Dafinov, J. Llorca, F. Medina and G. Rupprechter, *J. Catal.*, 2009, **263**, 239–246.

28 J. Yu, S. Liu and H. Yu, *J. Catal.*, 2007, **249**, 59–66.

29 (*a*) R. L. Zhang, J. Chang, Y. Y. Xu, L. R. Cao, Y. W. Li and J. L. Zhou, *Energy Fuels*, 2009, **23**, 4740–4747; (*b*) J. Gaube and H. F. Klein, *Appl. Catal., A*, 2008, **350**, 126–132.

30 (*a*) N. T. Thao, H. Alamdari, M. H. Zahedi-Niaki and S. Kaliaguine, *Appl. Catal., A*, 2006, **311**, 204–212; (*b*) X. J. Zhang, Y. Liu, G. Q. Liu, K. Tao, Q. Jin, F. Z. Meng, D. Wang and N. Tsubaki, *Fuel*, 2012, **92**, 122–129.

31 (*a*) G. P. Jiao, Y. J. Ding, H. J. Zhu, X. M. Li, J. W. Li, R. H. Lin, W. D. Dong, L. F. Gong, Y. P. Pei and Y. Lu, *Appl. Catal., A*, 2009, **364**, 137–142; (*b*) A. N. Pour, M. R. Housaindokht, S. F. Tayyari and J. Zarkesh, *J. Nat. Gas Chem.*, 2010, **19**, 107–116.

32 M. Gupta, M. L. Smith and J. J. Spivey, *ACS Catal.*, 2011, **1**, 641–656.

33 V. M. Lebarbier, D. Mei, D. H. Kim, A. Andersen, J. L. Male, J. E. Holladay, R. Rousseau and Y. Wang, *J. Phys. Chem. C*, 2011, **115**, 17440–17451.

34 H. T. Zhang, X. M. Yang, L. P. Zhou, Y. L. Su and Z. M. Liu, *J. Nat. Gas Chem.*, 2009, **18**, 337–340.

35 L. Dong, Z. Liu, Y. Hu, B. Xu and Y. Chen, *J. Chem. Soc., Faraday Trans.*, 1998, **94**, 3033–3038.

36 Z. H. Xiao, S. H. Jin, X. K. Wang, W. Z. Li, J. H. Wang and C. H. Liang, *J. Mater. Chem.*, 2012, **22**, 16598–16605.

37 H. H. Dong, M. J. Xie, J. Xu, M. F. Li, L. M. Peng, X. F. Guo and W. P. Ding, *Chem. Commun.*, 2011, **47**, 4019–4021.

38 K. Faungnawakij, R. Kikuchi, T. Fukunaga and K. Eguchi, *Catal. Today*, 2008, **138**, 157–161.

39 B. Bridier and J. P. Ramirez, *J. Am. Chem. Soc.*, 2010, **132**, 4321–4327.

40 C. H. Lu, L. M. Qi, J. H. Yang, D. Y. Zhang, N. Z. Wu and J. M. Ma, *J. Phys. Chem. B*, 2004, **108**, 17825–17831.

41 L. F. Chen, P. J. Guo, M. H. Qiao, S. R. Yan, H. X. Li, W. Shen, H. L. Xu and K. N. Fan, *J. Catal.*, 2008, **257**, 172–180.

42 A. Gervasini, M. Manzoli, G. Martra, A. Ponti, N. Ravasio, L. Sordelli and F. Zaccheria, *J. Phys. Chem. B*, 2006, **110**, 7851–7861.

43 R. K. Marella, C. K. P. Neeli, S. R. R. Kamaraju and D. R. Burri, *Catal. Sci. Technol.*, 2012, **2**, 1833–1838.

44 D. Kishore and A. E. Rodrigues, *Appl. Catal., A*, 2008, **345**, 104–111.

45 T. Grzybek, J. Klinik and B. Buczek, *Surf. Interface Anal.*, 1995, **23**, 815–822.

46 M. Y. Ding, Y. Yang, B. S. Wu, T. J. Wang, L. L. Ma, H. W. Xiang and Y. W. Li, *J. Mol. Catal. A: Chem.*, 2011, **351**, 165–173.

47 F. Wang, J. Huang, Y. Xu, L. Dai, D. Lu and S. Peng, *Chin. J. Catal.*, 1994, **15**, 426–431.

48 X. M. Yang, Y. Wei, Y. L. Su and L. P. Zhou, *Fuel Process. Technol.*, 2010, **91**, 1168–1173.